2020

Hierarchical Mechanisms of Lateral Interactions in High-Performance Fibers

Taylor A, Stockdale

Daniel P. Cole

Jeffrey M. Staniszewski

Michael R. Roenbeck

Dimitry Papkov

See next page for additional authors

Authors

Taylor A, Stockdale; Daniel P. Cole; Jeffrey M. Staniszewski; Michael R. Roenbeck; Dimitry Papkov; Steve R. Lustig; Youris A. Dzenis; and Kenneth E. Strawhecker

Research Article

Hierarchical Mechanisms of Lateral Interactions in High-Performance Fibers

Taylor A. Stockdale, Daniel P. Cole, Jeffrey M. Staniszewski, Michael R. Roenbeck, Dimitry Papkov, Steve R. Lustig, Yuris A. Dzenis,*,[#] and Kenneth E. Strawhecker*,[#]

Read Online

ACCESS | Metrics & More | Article Recommendations | Supporting Information

ABSTRACT: The processing conditions used in the production of advanced polymer fibers facilitate the formation of an oriented fibrillar network that consists of structures spanning multiple length scales. The irregular nature of fiber tensile fracture surfaces suggests that their structural integrity is defined by the degree of lateral (interfacial) interactions that exist within the fiber microstructure. To date, experimental studies have quantified interfacial adhesion between nanoscale fibrils measuring 10−50 nm in width, and the global fracture energy through applying peel loads to fiber halves. However, a more in-depth evaluation of tensile fracture indicates that fiber failure typically occurs at an intermediate length scale, involving fibrillation along interfaces between fibril bundles of a few 100s of nanometers in width. Interaction mechanisms at this length scale have not yet been studied, due in part to a lack of established experimental techniques. Here, a new focused ion beam-based sample preparation protocol is combined with nanoindentation to probe interfaces at the intermediate length scale in two high-performance fibers, a rigid-rod poly(p-phenylene terephthalamide) and a flexible chain ultrahigh molecular weight polyethylene fiber. Higher interfacial separation energy recorded in the rigid-rod fiber correlated with less intensive fibrillation during failure and is discussed in the context of fiber chemistry and processing. Power law scaling of the total absorbed interfacial separation energy at three different scales in the polyethylene fiber is observed and analyzed, and distinct energy absorption mechanisms, featuring a degree of self-similarity, are identified. The contribution of these mechanisms to the overall integrity of the fiber is discussed, and the importance of the intermediate scale is elucidated. Results from this study provide new insights into the mechanical implications of hierarchical lateral interactions and will aid in the development of novel fibers with further improved mechanical performance.
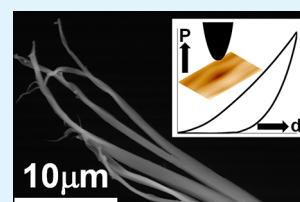
KEYWORDS: high-performance fiber, structure, fibrillar network, mechanical properties, processing

1. INTRODUCTION

High-performance fibers are utilized in many structural applications ranging from sporting goods to protective armor and aerospace primary structures. The high strength and stiffness exhibited by these fibers originates from a highly oriented hierarchical microstructure, which is developed during the drawing process of fiber production.[1−4] Variations in fiber processing conditions can directly contribute to changes in the fiber microstructure (e.g., crystallinity, molecular and supra-molecular orientation, core−shell development, etc.) and ultimately the bulk fiber properties.[3,5−7] Considerable resources have been dedicated to the development of fiber processing techniques that achieve optimum performance, but after years of research and development efforts, the theoretical strength of many high-performance fibers is yet to be realized.

Synthetic advanced polymer fibers, such as poly(p-phenyl-ene terephthalamide) (PPTA) and ultrahigh molecular weight polyethylene (UHMWPE), possess a complex hierarchy of structural features spanning multiple length scales.[2,8−13] As polymer chains orient and crystallize during spinning, crystallites are formed within discrete domains, often referred to as microfibrils, which measure 10−50 nm in width.[2,9,11,14] These microfibrils form bundles measuring 100−500 nm in width, and the fibril bundles ultimately make up the full fiber measuring 10s of micrometers in diameter. Regarding the nomenclature for these microstructural features, microfibril (a historically used term) may be misleading, due to their nanoscale widths. For clarity, these features will be referred to as nanofibrils. The fact that these nanofibrils form distinct bundles at the intermediate scale is interesting, and although the cause of this discretization has been scrutinized in early investigations, further studies are needed to elucidate the underlying mechanisms involved.[15,16] In the remainder of the text, we will refer to the characteristic nanofibril and nanofibril bundle scales as nanoscale and intermediate scale, respectively.

Advanced polymer fibers are utilized for their impressive tensile properties. The existence of hierarchical oriented microstructure implies the presence of extensive interfaces throughout the fiber microstructure. Therefore, fiber perform-
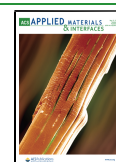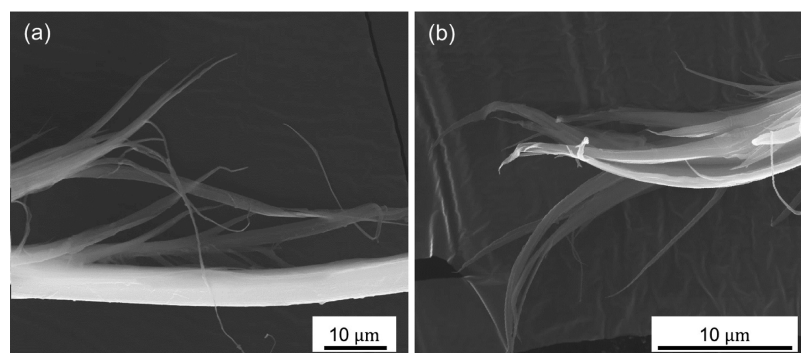
Figure 1. Tensile fracture surfaces of a PPTA fiber (a) and an UHMWPE fiber (b) demonstrating fibrillation along fibril bundle interfaces.

ance must be highly dependent on lateral interactions and effective load transfer across interfaces within the material hierarchy. Despite the importance of these interfaces, to date, very little has been done to experimentally measure interfacial properties in high-performance fibers.

At the nanoscale, interfacial properties can be measured using techniques such as atomic force microscopy (AFM). Recently, an AFM-based indentation study was conducted at the nanoscale, and the adhesive energy required to separate adjacent nanofibrils was measured in the UHMWPE fiber.[17] However, other experiments on high-performance fibers indicate the importance of interfacial properties at the intermediate scale, which is related to fibril bundles. Bulk mechanical properties of fibers are characterized through global mechanical techniques, such as single fiber tensile tests and transverse compression studies.[18−22] Examination of fiber fracture surfaces provides insight into the relevant length scales impacting bulk fiber behavior. Post-mortem analysis of fractured high-performance polymer fibers typically reveals extensive fibrillation, as shown in Figure 1. While nanofibril dimensions are 10s of nanometers in width, the fibrillated segments in Figure 1 are much wider. This indicates that failure occurs predominantly at an intermediate length scale related to bundles of nanofibrils. Thus, it is critical to understand the mechanics of nanofibril bundles, as well as the lateral interactions between bundles. However, to the authors' knowledge, no experimental work has been performed at this intermediate scale. The lack of information on the bundle scale also presents a challenge for modeling fiber deformation and failure behavior. Recent modeling efforts have highlighted the importance of interactions at the mesoscale in PPTA fibers,[23,24] but these interactions are yet to be experimentally characterized. Acquiring data at the intermediate scale is therefore needed to improve our understanding of hierarchical mechanical behavior in advanced fibers, which could be used to update existing models as well as develop new multiscale fiber models.

Due to the increased size of features at the intermediate scale, AFM is not suitable for characterizing interfacial properties. One technique that can be used is instrumented indentation. Referred to as "nanoindentation", this mechanical testing technique is used to probe material properties on the nano- to microscale. Compared to AFM-based nanoindentation, where tip radii are ∼10 nm and measured forces are in the nano-Newton range, nanoindentation uses larger probe tips (∼> 100 nm) and forces are often in the micro-Newton range or greater. In general, nanoindentation can be used for fiber surface characterization. However, there are several challenges

when applying nanoindentation to the external surfaces of fibers. First, classical indentation studies assume the material to be a flat, semi-infinite elastic half space,[25] but fibers possess surface curvature, which requires additional correction factors to properly interpret results.[26−29] In addition, the fiber exterior may generate different indentation response compared to the interior volume responsible for bulk mechanical behavior. For example, consider the complex skin-core microstructure of PPTA, where skins can extend radially for 100s of nanometers from the fiber surface.[9,30−34] Thus, characterizing the internal morphology and properties of the fiber is essential. Accessing a fiber's internal morphology by embedding it in a matrix and microtoming it has been utilized.[34,35] However, this technique is not ideal for isolating internal features for mechanical characterization because (i) nanoscale morphologies may be damaged through direct contact with the microtome blade and (ii) indentation measurements could reflect a combined response from the fiber and embedding matrix.[36−38] Thus, accessing the inherent fiber microstructure with minimal distortion is critical.

A novel sample preparation technique, which provides rapid access to the internal morphologies of high-performance fibers via fracturing after notching with a focused ion beam (FIB), has recently been developed.[39] The technique uses the FIB to introduce opposing notches in a single filament separated by a finite distance. This generates a longitudinal plane where fracture can easily propagate, yielding two mirrored samples with an exposed interior. Effective mounting of the exposed surface was followed by advanced AFM imaging to create high-resolution topography and mechanical property maps of hierarchical interior fiber morphologies.[6,13,39−41] FIB milling was performed to create end notches, thus all property measurements were made more than 5 μm from the ion-affected regions, which likely eliminated any ion induced property changes to the fibers.[42] Samples prepared by this technique were also suitable for characterizing interfacial properties at the nanoscale in UHMWPE, as mentioned above.[17] Another investigation, which evaluated interfacial properties at a much larger length scale, utilized a variable angle, single fiber peel test on UHMWPE fibers to measure the effects of fiber structure on failure.[43] While these two studies evaluate lateral mechanisms at the nano- and macro-scale, no such information exists at an intermediate scale. Obtaining measurements from this mesoscale will enhance the understanding of multiscale fiber behavior and will serve as a bridge between highly local behavior and global fiber response.

Here, such an intermediate scale has been studied by nanoindentation. Significantly larger forces are utilized,

rendering samples made by the previous FIB-based method inadequate due to issues with rigid mounting of the end of a separated fiber half. A new sample preparation and mounting protocol was developed to expose the internal morphology of a nonseparated high-performance fiber, enabling higher load probing while the sample remained rigidly mounted under tension. Interfacial nanoindentation experiments were conducted on two different high-performance fiber types to gain insight into nanofibril bundle interactions and their connections with fiber chemistry and processing. Experimental results at the intermediate scale were analyzed and compared with nanoscale and macroscale fiber behavior. Lateral interactions at different length scales were evaluated, and underlying mechanisms providing structural integrity to the fiber were proposed.

2. EXPERIMENTAL SECTION

2.1. Materials and New Sample Preparation Method. Two different types of ballistic fibers were analyzed in this study; PPTA (Kevlar KM2, 600 denier) and UHMWPE (Dyneema SK76, 1350 denier). Individual fibers were teased from the tows and used as received. The remainder of the paper will refer to these fibers as PPTA and UHMWPE, respectively.

In the previous samples prepared by FIB-based notching, two reciprocal notches were milled transverse to the fiber axis so that pulling the fiber ends resulted in complete separation of the fiber into two parts. Rigid mounting of such samples for nanoindentation is problematic because (i) lack of fixed boundary conditions would lead to large rotational tendencies due to increased loads from nanoindentation and (ii) the previously utilized substrate (i.e., double-sided adhesive), while being sufficiently rigid for low force AFM characterization, would be too compliant for nanoindentation studies. To circumvent these issues, a new sample preparation technique was developed where a T-shaped notch geometry was established and utilized on a rigidly mounted fiber under tension followed by effective peeling to expose the interior of the fiber.

An individual fiber was draped over the curved surface of a glass vial (2.0 mL, 1 cm diameter) and small masses (~1 g) were attached to either end to provide constant tension over the fiber length. Two small drops of adhesive were applied to the fiber near the top of the vial, separated by ~5 mm, and excess fiber was cut away after curing. Further details of the mounting procedure can be found elsewhere.[28] Once securely mounted, the fiber exterior was sputter coated with ~30 nm of Au−Pd to prevent charging effects during the notching procedure. The mounted fiber was fixed to a 45° SEM stub, and then the SEM stage was tilted to 7°, shown schematically in Figure 2a, positioning the fiber orthogonal to the FIB. In this configuration, inverted T-shaped notches were milled into the top half of the fiber. Ga+ ion milling was utilized (FEI Nano V600 dual beam) with milling parameters of 16 kV and 0.47 nA. The geometry and placement of the notches in this study, shown in Figure 2b,c, yield a sample which can be peeled open to provide access to the fiber interior while the fiber remains intact and in solid contact with the underlying glass substrate.

After milling, the vial was placed on an optical microscope stage equipped with x, y, and z-translation capability. A micromanipulator stage, also with x, y, and z-translation, was positioned near the microscope. A scanning tunneling microscope (STM) probe (platinum/iridium solid wire, 0.25 mm diameter, Bruker) was sectioned with a wire cutter to produce a long, tapered edge, which was suitable to insert into the side of the T-shaped notch. The probe was adhered to the end of a rigid beam which was fixed on the micromanipulator stage. The fiber was brought into focus under a 50× objective lens and was positioned so the observer viewed directly into the vertical portion of the T-shaped notch. By adjusting the micromanipulator stage, the STM probe was carefully inserted into the horizontal portion of the notch and, in a simultaneous motion, the microscope stage was translated to simulate a peeling motion, shown schematically in Figure 2d. To limit contact with the newly created
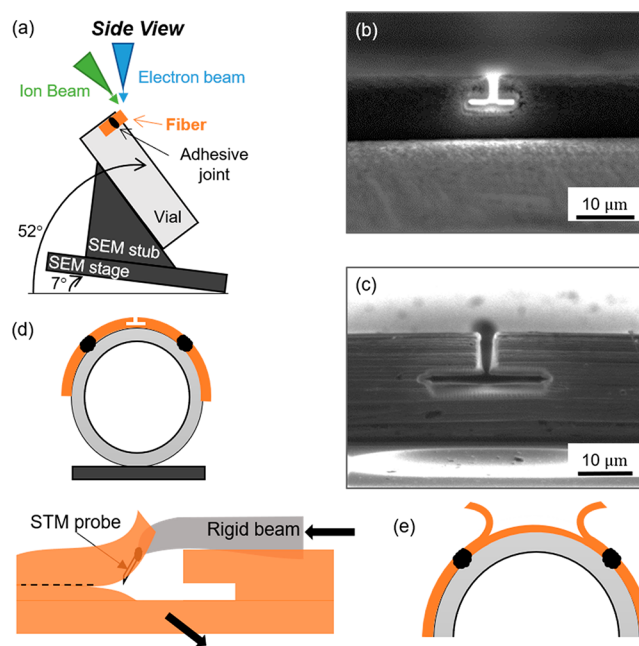

Figure 2. New FIB-notch sample preparation technique demonstrating fiber positioning for ion milling (a) and FIB images of corresponding T-shaped notches milled into single PPTA (b) and UHMWPE (c) fibers. The narrow notches at either end of the horizontal notch in the UHMWPE fiber help facilitate crack propagation along the fiber axis while peeling. A schematic of the peeling procedure is shown in (d) with the final specimen ready for nanoindentation shown in (e).

internal surface, the stage was translated such that the STM probe only contacted the internal face of the top side of the peeled section. This was repeated on both sides of the T-shaped FIB-notch, which produced a specimen with an exposed interior suitable for subsequent nanoindentation studies, shown schematically in Figure 2e. In addition to accessing internal fiber morphologies without through-thickness fracture, the T-shaped notches allow much larger fiber sections to be prepared compared to previous notch geometries.[6,13,39] The peeling generated internal surfaces extending ca. 1 mm along the fiber axis. Due to the fibrillar nature of the fiber microstructure, the resulting fiber surfaces were not planar.

2.2. Probing Interfaces Between Fibril Bundles. Quasi-static nanoindentation was performed on internal fiber morphologies using a Hysitron TI-950 Triboindenter with a 60° sphero-conical diamond probe tip (350 nm tip radius). Prior to local mechanical testing, the indenter probe was raster scanned over the exposed surface to map the topography of the fiber interior (10−15 μm scan size, 0.4−0.5 Hz scan rate, 1.0 μN set point). Image sizes and scan locations were adjusted to maximize the capture area while avoiding the edge of the fiber. Indentations were performed in displacement control using a triangular loading scheme with a 10 s loading segment followed by a 10 s unloading segment. Indentation depths of 150, 300, and 500 nm were selected for this study.

Due to the increased size of the indenter probe and depth of indentation, much higher forces are applied to the sample surface compared to AFM-based indentation. Such forces, if applied away from the geometric center of the sample, which is equivalent to a half cylinder mounted on a flat substrate, could cause fiber rotation due to torsional moment. This would contribute an additional compliance to the measured indentation response. This structural compliance can vary as a function of position within the specimen.[38] One strategy for estimating structural compliance is by empirical measurements and correlations, as was done by Stone, Yoder, and Sproul (SYS).[44] Here, three arrays of equally spaced indentations were performed across the width of each initially imaged location at set depths of 150, 300, and 500 nm, respectively. Details for constructing the SYS plot, and results
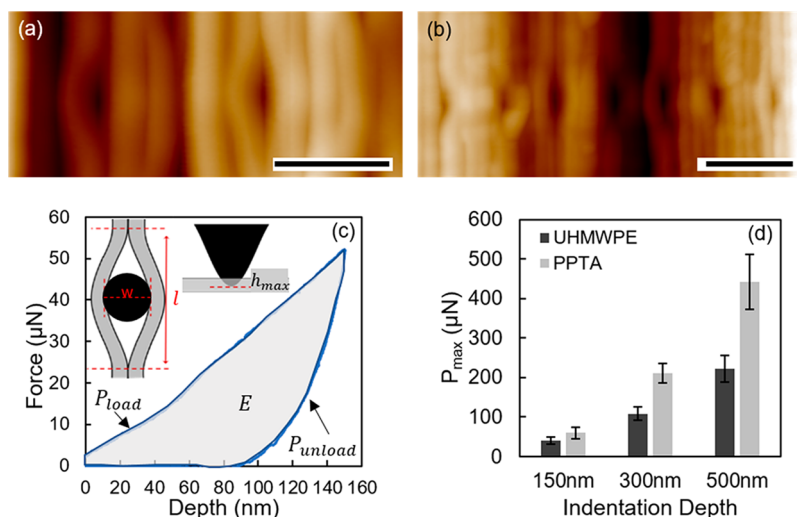
Figure 3. Raster scan images of fiber interior after indentation exhibiting discrete fibril bundles in UHMWPE (a) and PPTA (b) fibers; scale bars are 2 μm. A representative load−displacement plot for a 150 nm indent (c) with schematics defining measurements from residual indentations for energy normalization (inset (c), used with permission from ref 17.). Peak load results for indentations performed between fibril bundles (d). Error bars indicate one standard deviation.

from the structural compliance determination for this study can be found in the Supporting Information (SI). From this analysis, a narrow strip exhibiting minimal compliance is identified for subsequent indentation experiments (i.e., in this region, rotation due to indentation can be assumed negligible). Representative raster scans of the interior of two distinct fiber types after performing structural compliance indents are shown in Figures 3a,b. In both fibers, well-defined highly oriented fibril bundles measuring a few 100s of nanometers in width are clearly distinguishable.

Once the suitable indentation region was identified, a new location along the fiber length was raster scanned and interfaces between fibril bundles were identified. In these newly scanned areas, automated indentation scripts were utilized, where user-defined locations between fibril bundles were selected for subsequent indentation. Series of indents were performed between fibril bundles to measure properties related to interfacial interactions. Two sets of indentations were performed in this study: single and repeated indents. The latter indentation sets were utilized to partition the total indentation energy due to different energy dissipation mechanisms. The loading scheme was adjusted from a single triangular load scheme to a sawtooth load scheme with multiple loading and unloading cycles of constant amplitude within a single experiment. Multiple data sets were collected between the two fiber types, and statistical analysis was performed to verify any observed trends. Unless noted otherwise, all image analysis of surface morphologies was carried out using Fiji, a distribution of ImageJ.[45,46]

3. RESULTS

3.1. Load−Displacement Response During Interfacial Indentation. In nanoindentation, load−displacement (P−h) data are recorded continuously during loading and unloading and subsequently analyzed to extract material properties such as hardness and elastic modulus. Parameters typically extracted from the P−h curves include the maximum load, P_{max}, maximum indentation depth, h_{max}, and contact stiffness, $S = dP/dh$, defined as the slope of the upper portion of the unloading curve during initial unloading.[47] A representative load−displacement curve for a 150 nm indentation is provided in Figure 3c. The contact depth, h_c, is given by eq 1, defined as the depth along which contact is maintained between the probe and sample during indentation:

$$h_c = h_{max} - \epsilon(P_{max}/S) \tag{1}$$

where ϵ is a constant related to indenter geometry. Typical values are 0.75 for a paraboloid of revolution and 1.00 for a flat punch.[48] Traditional hardness measurements assume samples to be flat, isotropic and homogeneous. Deviations from these conditions may render different values based on sample geometry and the degree of elastic recovery after unloading.[25,26,28,29,47] The samples evaluated in this study possess a hierarchical microstructure, nonflat surface profiles, and exhibit highly anisotropic properties, thus violating many of these classical nanoindentation assumptions. In lieu of measuring the hardness, which would require an accurate measure of the contact area as the indenter probe is inserted into a highly complex microstructure, the peak load measured at each indent depth will be utilized for analyzing fibril bundle separation behavior. Indentations were performed between fibril bundles at three indentation depths (e.g., 150, 300, and 500 nm), and each experiment was conducted at a new location. Peak loads were obtained at each depth for both fiber types and results are presented in Figure 3d. The peak loads achieved at each indent depth were greater for PPTA compared to UHMWPE with values measuring 51%, 94%, and 98% higher at 150, 300, and 500 nm depths, respectively.

After each set of indents was performed, the topography of the indented surface was again mapped by raster scanning to observe residual indentations, see Figure 3a,b. The total energy required to produce the observed residual indents was calculated by integrating the area between the load and unload curves in the load−displacement plot, see highlighted region in Figure 3c.[17,49] This energy, E, is given by eq 2

$$E = \int_0^{h_{max}} P_{load}\, dh - \int_0^{h_{max}} P_{unload}\, dh \tag{2}$$

Following the protocol from a similar study using AFM-based nanoindentation,[17] the area-normalized indentation energy, E_{area}, was approximated on a unit area basis where the split area was defined as the product of the residual indent length, l (as measured from images obtained from raster scans post indentation), and h_{max}, shown schematically in the inset of Figure 3c. Values for E_{area} were calculated using eq 3
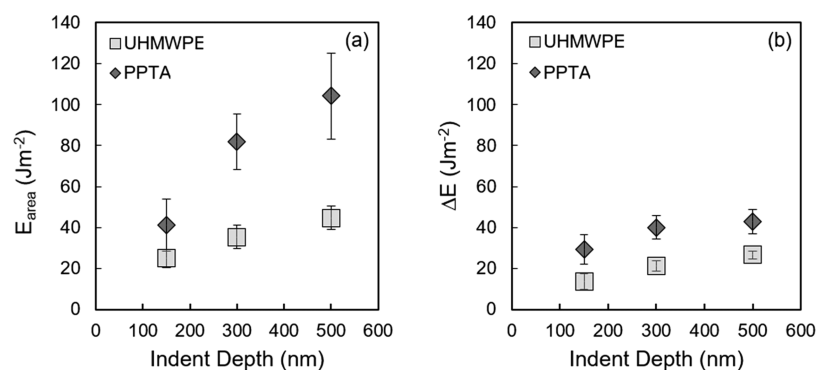
Figure 4. Normalized indentation energy results for UHMWPE (squares) and PPTA (diamonds) fibers from indents performed between fibril bundles. E_{area} results in (a) are from single indents based on eq 3 while ΔE results in (b) are based on the energy difference obtained through repeated indent experiments and calculated using eq 4. Error bars indicate one standard deviation.
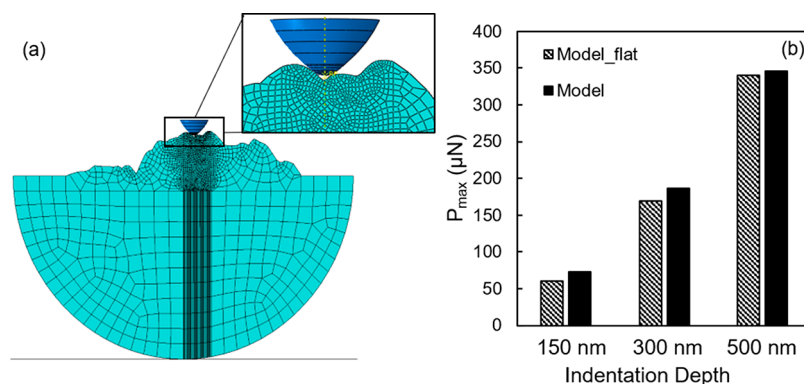

Figure 5. FEM model used to analyze effects of sample topography on indentation response (a) and simulation results showing diminishing surface topography effects with indentation depth (b).

$$E_{area} = E/(l \times h_{max}) \tag{3}$$

Normalized indentation energy results for single indents are presented in Figure 4a. At each indentation depth, the normalized indentation energy for PPTA is approximately double that observed for UHMWPE.

3.2. Evaluation of Absorbed Interfacial Separation Energy Based on Repeated Indents. During the indentation, several energy dissipation mechanisms may occur simultaneously. For example, energy could be dissipated through fracture along bundle interfaces and through frictional contact within the tip−sample interaction volume surrounding the probe tip. Following the work by McDaniel et al.,[17] the total energy dissipated during indentation was partitioned by analyzing results from repeated indentations in the same location. Upon withdrawing the probe after the first indent, partial elastic recovery occurred, as evidenced by the nonzero area under the unload curve in Figure 3c. A second indent was subsequently performed in the same location and to the same depth, which yielded a considerable decrease in E (∼50−60%). The integrated area from the second indent provides information regarding the energy dissipated through frictional contact within the tip−sample interaction volume, as well as the energy required to overcome intermolecular forces initiated as the separated bundles come together due to elastic recovery. A third indent was also performed in the same location, which yielded load−unload curves similar to the second indent but measured an additional decrease in E (∼10−15%). The similar indentation response between repeated indents indicates a possible time-dependent, elastic energy dissipation mechanism

related to relaxation of the microstructure between subsequent indents. Subtracting indent energies from the first and second indents yields a more accurate measure of the energy absorbed during the formation of the observed residual indent. This energy difference, or absorbed energy, is estimated by eq 4

$$\Delta E = E_{absorbed} = (E_1 - E_2)/(l \times h_{max}) \tag{4}$$

where E_i is the integrated energy from the first and second indents, defined by eq 2. Repeated-indent experiments were performed between fibril bundles for both fiber types and the results, based on eq 4, are shown in Figure 4b. After evaluating the energy differences, PPTA absorbs approximately twice the energy of UHMWPE at each indentation depth.

3.3. Analysis of Effects of Sample Topography. Generally, indentation studies are performed on flat substrates. However, this study performs indents in a groove between two fibril bundles. To study potential effects of sample topography on the measured indentation response, finite element representation of PPTA fiber surface profiles was created. A spline was fit to a series of data points taken from the experimental surface profiles and features approximating a location between two bundles were aligned with the centerline of a half cylindrical fiber. The resulting model, shown in Figure 5a, was meshed according to the details in the SI. To account for the fiber mechanical properties, the model was calibrated using experimental results from 150 nm indents on a relatively flat area of a PPTA fiber with minimized structural compliance. Computational predictions for max loads from indentations at each depth on a flat half cylinder were compared to indentation simulations on samples possessing actual complex
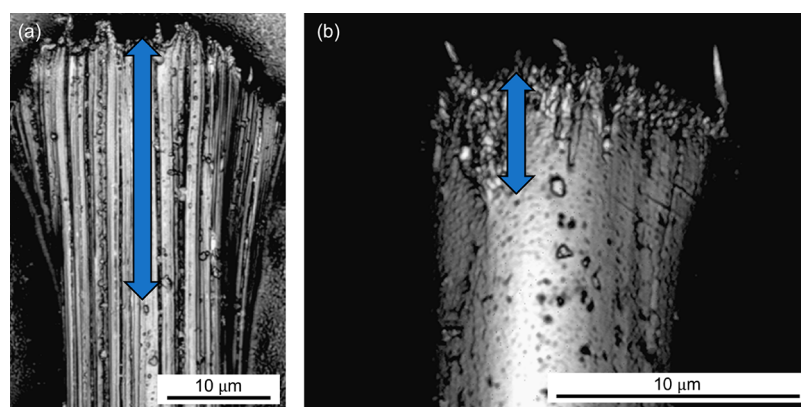
Figure 6. Fibrillation observed in UHMWPE (a) and PPTA (b) fiber fracture surfaces after fiber bending experiments. Separation of nanofibril bundles extends much farther along the fiber length in UHMWPE compared to PPTA, as indicated by the double arrows along the fiber axis.

topography, and the results are presented in Figure 5b. Compared to simulation results on a flat half cylinder, simulations between two fibril bundles increased the load measured from the indenter by 22%, 10%, and 2% for depths of 150, 300, and 500 nm, respectively. The enhanced load is most pronounced for shallower indents and indicates possible additional contributions to the measured indentation response due to surface effects. Effective interpretation of results from shallow indents would require additional correction factors, but deeper indents indicate that these surface effects diminish with increasing indentation depth. Note that 3D FEM models of half-fibers, similar to the one presented here, can be used to evaluate torsional rigidity and structural compliance of the samples during indentation at various distances from the sample center, thus further improving accuracy of the extracted data.

4. DISCUSSION

4.1. Strength of Intermediate-Scale Lateral Interactions in UHMWPE and PPTA Fibers. The fibers evaluated in this study consist of two very different polymers. Each represents a distinct high-performance polymer fiber class based on characteristics of the macromolecular chains—flexible versus rigid-rod for UHMWPE and PPTA, respectively. These two fibers are also produced using different fabrication techniques. Surprisingly, despite these differences, the polymers yield high-performance fibers with comparable tensile properties. In addition, each fiber possesses a similar hierarchical structure with reported nanofibril widths measuring 20−50 nm and fibril bundles measuring 200−600 nm.[2,6,13,35,41]

Analysis of data presented in Figures 3d and 4a,b indicate that more energy is required to separate fibril bundles in PPTA fiber compared to UHMWPE fiber. The larger peak loads observed in PPTA and correspondingly smaller residual interfacial split areas lead to higher normalized separation energy values.

In general, an increase in macromolecular rigidity can be expected to result in an increase in interfacial brittleness. That is, more rigid molecules should yield longer interfacial fracture lengths. However, the opposite effect was observed in experiments, which indicates that other mechanisms of lateral interaction must be present.

Different lateral interactions can be a result of differing manufacturing processes for the distinct fiber types. The final

processing step during fiber formation, which involves solvent extraction, is critical for the development of the fiber microstructure and is not yet fully understood. For UHMWPE fibers produced by gel-spinning, quenched fibers are subjected to additional drawing at elevated temperatures, which allows the flexible macromolecular chains to transition from a lamellar structure to a highly extended-chain structure.[3,4,50,51] In contrast, PPTA fibers are produced by a dry jet−wet spinning technique, where the rigid-rod macromolecules are preferentially oriented by shear flow of the solution through the spinneret and, subsequently, the solution is drawn through a small air gap before entering a coagulation bath.[52] Upon entering the bath, a large-scale mass diffusion process takes place, removing approximately 80% of the initial spinning solution, before the fiber is washed and subjected to additional thermal treatment.[53] In both fiber types, the combination of large mass flux and oriented crystallization processes leaves microscopic voids within the fiber microstructure as well as a fibrillar network, which has been identified through various scattering and direct imaging techniques.[12,15,16,54−58]

In the case of PPTA, spinning of the liquid crystalline dope is followed by phase separation and spinodal decomposition as the coagulant slowly diffuses into the fiber.[59] This can result in shorter and more interconnected crystals compared to UHMWPE. The latter is indirectly supported by lower reported crystallinity of PPTA fibers (e.g., 70−80%) compared to UHMWPE fibers (e.g., 90−95%).[60−63] High crystallinity of UHMWPE presumes longer, more perfect fibrils, with less disorder that can otherwise increase lateral interaction. This can explain lower observed interfacial separation energy in UHMWPE.

On the basis of the new experimental data obtained in this study, one can expect that UHMWPE fibers have a higher propensity to fibrillate upon macroscopic failure. To assess this, PPTA and UHMWPE fibers were fractured macroscopically by bending individual filaments over a razor blade. During bending, compression loading is experienced on the bottom portion of the fiber, below the neutral axis, while tensile loading occurs in the upper portion of the fiber. Ultimately, shear deformation leads to fibrillation, which is shown in Figure 6. Comparison of fiber fracture surfaces shows that both fibers exhibited extensive fibrillation at the intermediate scale. However, separation of the nanofibril bundles propagated much farther along the fiber length in UHMWPE compared to PPTA, as evidenced by the apparent increase in fiber diameter

Table 1. Average Absorbed Energy (ΔE) Results from Indents between Fibril Bundles in This Study Compared to ΔE Results from Indents between Individual Nanofibrils Using AFM-Based Nanoindentation[17]

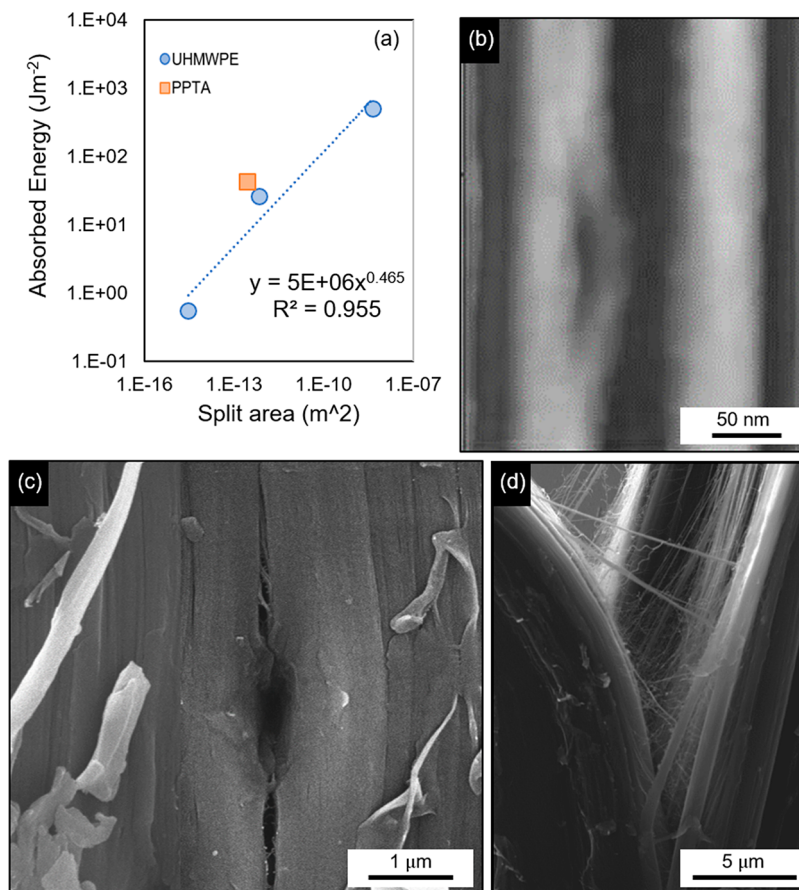|	indentation depth		
	150 nm/30 nm	300 nm/40 nm	500 nm/50 nm
ΔE − fibril bundles (J m^{-2})	13.5	21.3	26.6
ΔE − nanofibrils (J m^{-2})	0.52	0.55	0.34

Figure 7. Power law scaling of the total absorbed energy and corresponding split area in UHMWPE fibers (a). The data point for the intermediate scale considers only the 500 nm depth results, as this depth is sufficient to neglect surface effects according to FEM results. Values for total absorbed energy in the single fiber peel test were calculated from geometry and reported energy release rate values from ref 43. Crack images illustrating variation in size and frequency of lateral connections at increasing length scales ranging from nanofibril separation (used with permission from ref 17) (b), to nanofibril bundle separation (c), and full fiber splitting (d).

near the fibrillated fractured end, indicated by double arrows in Figure 6.

Similar differences in fibrillation behavior have been observed for these two fiber types under other loading configurations. One study evaluated the transverse tensile strength of UHMWPE, PPTA, and polybenzoxazole (PBO) fibers and found that the critical load to initiate fiber splitting was about 50% lower for flexible-chain UHMWPE fibers compared to rigid-rod PPTA and PBO.[64] Other studies measuring the transverse compression response of UHMWPE and PPTA fibers have been performed to evaluate deformation mechanisms under transverse loading conditions.[21,22,32] While fibrillation occurred in both fiber types, the apparent cross-sectional area increased considerably with increased compressive strain for UHMWPE fibers, but remained largely unchanged in PPTA. The apparent area increase in UHMWPE was attributed to the development of new nanoscale voids with increasing compressive strain. In addition to new void

formation, AFM images of transversely compressed fibers indicated large-scale reorientation of a meso/nanoscale fibrillar network in UHMWPE that was not observed in PPTA.[22]

Together, these results indicate that the lateral interactions at the intermediate scale in rigid-rod PPTA fibers are stronger compared to those in flexible-chain UHMWPE fibers. The exact molecular and supramolecular mechanisms responsible for differences in lateral interactions and their dependence on manufacturing parameters need to be further studied. The separation energy measured here at the intermediate scale for the first time provides a quantitative measure that can be used for further comparative studies, manufacturing optimization, as well as development of next generation multiscale fiber failure models.

4.2. Analysis of Interfacial Separation Energies at Different Scales. To gain further insight into lateral interactions at different length scales within the fiber structural hierarchy, the measured intermediate-scale energy dissipation

behavior from this study was compared to previously reported experiments evaluating similar mechanisms in UHMWPE fibers at the nanoscale.[17] Comparison of these two studies revealed that magnitudes of the measured area-normalized absorbed energies at the intermediate scale (nanoindentation) were considerably larger (∼1−2 orders of magnitude) compared to those obtained at the nanoscale (AFM), see Table 1.

The absorbed energy (ΔE) results were also compared with energy values obtained from macroscopic single fiber peel tests performed on UHMWPE fibers. An equivalent absorbed energy, fracture energy in this case, was calculated based on sample geometry (i.e., fiber diameter and length of crack extension) and reported strain energy release rate values.[43] The total absorbed energy at each of the three length scales is plotted as a function of the corresponding split area in Figure 7a. Further significant increase of separation energy is observed at the macroscale, compared to the intermediate scale. A power law function was used to approximate the energy scaling behavior:

$$\Delta E \propto \text{split area}^{\gamma}$$

with the power exponent γ estimated to be 0.47. The AFM and indentation experiments that produce Figure 7a measure the area of residual crack propagated. However, what is unknown is the actual affected volume including a network structure that is producing the energy measurements. Therefore, the energy measured has greater certainty than the area measurements in the abscissa of Figure 7a. Nevertheless, it is expected that the overall trend should remain: much larger energies as the interaction area increases.

The dramatically different magnitudes of the absorbed energy at different length scales imply that different mechanisms of lateral interaction must be responsible for nano- and intermediate-scale separation, and for macroscopic splitting of the fiber. In general, forces resisting interfacial separation comprise a number of physical intermolecular (adhesive) interactions as well as chemical interactions. As polymers processed into fibers are typically fully polymerized and no additional chemical reactions are expected during fiber spinning and final structure formation, formation of chemical links between the hierarchical features is unlikely. However, a progressing interfacial crack can turn into a cohesive fracture crack propagating inside the adherend. In the context of axially oriented hierarchical features of the high-performance polymer fibers, the latter would require polymer chain scission and, as a result, would demand significantly higher energy. Conversion from adhesive to cohesive fracture is often observed in adhesive joints with planar interfacial geometry that correspond to energetically favorable planar cracks. Interfaces between mostly cylindrical, oriented features in the high-performance fibers are not planar. However, even slight variation in feature orientation can cause a degree of entanglement, leading to features crossing the interfacial crack path creating a crack bridge. Such bridges can lead to crack tip shielding and their eventual breakage (primarily in tension, directed along the strongest polymer chain orientation direction) would consume significant amounts of energy. Typical observations of interfacial cracks at the three scales in the UHMWPE fiber are shown in Figure 7b−d.

At the nanoscale (in the AFM-based indentation study), the energy required to separate nanofibrils was low,[17] indicating this ultrafine scale of separation is not sufficient to engage significant lateral bridging. Observation of residual indents from the AFM study supports this notion (see Figure 7b). Note that due to the relatively low image resolution, there might still have been small, molecular level ties (bridges) not visible at the scale of observation.

At the intermediate scale, i.e., in our current nano-indentation study, much higher energy values were recorded. With a much larger tip−sample interaction volume and applied forces, compared to AFM-based indentation, enough separation was created to engage lateral connections between adjacent fibril bundles. Evidence of the latter mechanism is provided in Figure 7c, where crack extension from the vertical edges of the residual indentation is clearly visible. Several nanofibril bridges are observed spanning across this extended interfacial crack between the nanofibril bundles and some nanofibrils have fractured in the process.

Considering the macroscale peel test, absorbed energy values were further significantly increased, compared to the intermediate scale. Observation of the region near the crack tip in a peeled fiber indicates a significant increase in the number of nanofibril bridges, as shown in Figure 7d. In addition to the increased quantity of bridging features, an increase in the size of bridging features is observed, with some bridges reaching the fibril bundle size. This crack bridging mechanism is comparable to the toughening mechanism of collagen fibril bridging observed in bone.[65] While crack propagation along the length of the fiber may not require as much energy (i.e., separation of bundles), the increased separation through Mode-I opening causes reorientation of the bridging features such that they are loaded in tension, requiring significantly more energy to ultimately fracture. From this multiscale analysis, the dramatic increase in absorbed energy can be related to the number and size of lateral bridges that become engaged with increasing separation distance.

Note that the absorbed energy scales as a power law with the split area (Figure 7a). Power law scaling is observed in many physical phenomena and is often associated with self-similarity.[66] Images in Figure 7b−d indicate a degree of self-similarity in the crack geometries that may indicate self-similarity of lateral toughening mechanisms in fibers at different scales. Fractal scaling of oriented topographic features on surfaces of advanced fibers has been observed in the scale range from 100 to 4000 nm.[67] The scaling exponent is an important parameter that depends on hierarchical geometry and can be influenced by anisotropic inhomogeneity.[68] More studies are needed to elucidate the observed multiscale mechanisms, but the discovered scaling opens up intriguing possibilities of new approaches to fiber failure analysis.[69]

4.3. Why Do Advanced Fibers Fibrillate at an Intermediate Scale During Tensile Failure?
Fibers are designed to carry load primarily in tension. They buckle under compression and provide little resistance to torsion/shear loading (unless incorporated into composites). In most high-performance polymer fibers, tensile failure typically results in fibrillated fracture surfaces exhibiting features at the scale of nanofibril bundles, as illustrated in Figure 1. From Figure 7a, the magnitude of the normalized absorbed energy at the bundle (or intermediate) scale is larger than the energy absorbed during creation of the interfacial crack between nanofibrils (nanoscale). A "weakest link" failure theory would suggest that failure in these high-performance fibers should occur through the lowest energy absorption mechanism (i.e., separation of individual nanofibrils). Why, then, does

fibrillation due to tensile failure occur predominately along fibril bundle interfaces?

It is conceivable that the very low energy obtained from AFM-based indentation only materializes from highly local measurements at the nanoscale. In other words, separation along nanofibril interfaces cannot be sustained over indefinite lengths, which implies that nanofibrils only possess high degrees of orientation over a finite distance. Through various mechanisms during fiber spinning, nanofibrils can crystallize oblique to the fiber direction and cross with adjacent nanofibrils. In three-dimensions, this local misorientation can result in nanofibrils becoming entangled within confined volumes—in this case bundles measuring 405 ± 133 nm and 633 ± 184 nm in width for PPTA and UHMWPE, respectively. This mechanism also gives rise to the possibility of nanofibrils crossing between neighboring bundles (Figure 7c), although this crossing event would be much less prevalent. It follows that nanofibril bundles could also cross along the length of the fiber, though this would occur over much greater lengths compared to the local crossing of nanofibrils.

Evidence of fibril bundle misorientation along the fiber length is shown by bundles crossing the crack plane in Figure 7d. Advancement of the crack requires that these bridging bundles eventually fracture, which causes further increase in energy absorption, as indicated in Figure 7a. However, note that fracture behavior in the single fiber peel test (Figure 7d) is different compared to tensile failure. In tension, the applied load is evenly distributed along the fiber length, but due to structural inhomogeneities within fibril bundles, a distribution of stresses develops within the fiber microstructure. This stress variation is further compounded with variation of local strength of bundles, leading to gradual accumulation of fibril bundle breaks. These breaks occur in different fiber cross sections. Once a particular region of the fiber is sufficiently weakened by the accumulated bundle breaks, the remaining intact bundles become overstressed and deform through failure, some (apparently) undergoing plastic deformation and necking. During this final failure stage, which results in complete fiber separation into two parts, only relatively short bundle segments need to be pulled out from the surrounding fiber volume. Bundle entanglements at these relatively short length scales do not have significant effect on bundle pull-out.

Conversely, in the peel (macroscale) fracture, the crack is extended over a sizable length along a predetermined failure plane. Such a crack inevitably encounters individual nanofibrils and fibril bundles crossing the projected crack plane. Even slight relative misorientation of the bundles may be sufficient to cross the crack plane. In addition, unlike tensile fiber failure, the nanofibrils and fibril bundles bridging the crack are initially intact (i.e., lateral separation does not initially generate significant tensile stresses in fibrils bridging between the two peeled fiber halves). This creates strong bridging and crack shielding effects that are further augmented by gradual bridge reorientation as the crack face separation increases.

Note that the above interpretation of bundle-level fibrillation during macroscopic tensile failure requires strong, intimately bound nanofibril bundles. The latter can be held together by either internanofibrillar tie-chain molecules, or nanofibril entanglements caused by supra-nanofibrillar architecture. Examples of the latter include twisting, or wrapping, creating a random "weave". The characteristic length of such a weave is likely to be large, as nanofibrils appear randomly distributed in radial cross-sectional images.[22,35] Yet it should be short enough

to preserve fibril bundle action as a cohesive structural unit. Establishing characteristic lengths governing nanofibril and fibril bundle turns and entanglements within the fiber structure would be critical for further understanding and quantifying their effects on fiber failure behavior. The results of the current work provide new motivation to investigate such microstructural arrangements.

Finally, the tensile fracture of individual nanofibril bundles may generally exhibit failure mechanisms hierarchically similar to the full fiber failure. That is, nanofibril breaks may accumulate, followed by nanofibril pull-out. These effects might be masked by plastic necking that occurs at the bundle scale (see Figure 1). Direct in situ observation of tensile failure of nanofibrils and fibril bundles would be invaluable for further elucidation of the underlying mechanisms involved.

5. CONCLUSIONS

In this work, the lateral interaction mechanisms between fibril bundles within UHMWPE and PPTA fibers were probed using nanoindentation. A modified FIB-notch technique enabling more stable, tension-assisted sample mounting procedure was developed and implemented to gain access to the inherent internal morphology of individual fibers for subsequent local property measurements. The indentation results showed stronger separation resistance in PPTA fiber, compared to UHMWPE, which corroborated observed differences in fibrillation tendencies of these fibers during failure.

Analysis of absorbed separation energy in UHMWPE fiber at three different scales resulted in the first observation of scaling of lateral behavior in an advanced fiber. This scaling correlating with apparent self-similarity of lateral interfacial crossings at different length scales can lead to entirely new fiber models based on fractal mechanics.

The methodologies developed in this study provide critical insight into the size and interaction characteristics of fibril bundles at the intermediate scale that appears to be prevailing in fibrillation of many high-performance fiber families (e.g., liquid crystalline polyester, PBO, poly(p-phenylene benzobisthiazole) (PBZT) fibers, in addition to the studied PPTA and UHMWPE). It is clear from macroscopic failure analysis that the size and frequency of lateral connections between bundles have a profound impact on the mechanical behavior of fibers. Results from this study can lead to enhanced multiscale fiber models for predictive failure analysis of high-performance fibers. This will, in turn, continue to advance our understanding of the complex processing−structure−property relationships in advanced fibers. Future studies focused on understanding load transfer across these different length scales can lead to improved performance of existing fibers as well as development of novel fibers.

■ ASSOCIATED CONTENT

Ⓢ Supporting Information

The Supporting Information is available free of charge at https://pubs.acs.org/doi/10.1021/acsami.9b23459.

Statistical analysis; structural compliance determination; and finite element model development (PDF)

■ AUTHOR INFORMATION

Corresponding Authors

Yuris A. Dzenis − *Mechanical and Materials Engineering Department, University of Nebraska−Lincoln, Lincoln,*

Nebraska 68588, United States; ⓘ orcid.org/0000-0002-6645-3294; Email: ydzenis@unl.edu

Kenneth E. Strawhecker − *U.S. Army Research Laboratory, Weapons and Materials Research Directorate, Aberdeen Proving Ground, Maryland 21005, United States;* ⓘ orcid.org/0000-0002-3462-4757; Email: kenneth.e.strawhecker.civ@mail.mil

Authors

Taylor A. Stockdale − *Mechanical and Materials Engineering Department, University of Nebraska−Lincoln, Lincoln, Nebraska 68588, United States;* ⓘ orcid.org/0000-0002-7509-8466

Daniel P. Cole − *U.S. Army Research Laboratory, Vehicle Technology Directorate, Aberdeen Proving Ground, Maryland 21005, United States;* ⓘ orcid.org/0000-0002-8160-6156

Jeffrey M. Staniszewski − *U.S. Army Research Laboratory, Weapons and Materials Research Directorate, Aberdeen Proving Ground, Maryland 21005, United States;* ⓘ orcid.org/0000-0002-2469-3257

Michael R. Roenbeck − *Department of Marine Engineering, U.S. Merchant Marine Academy, Kings Point, New York 11024, United States;* ⓘ orcid.org/0000-0003-3446-6653

Dimitry Papkov − *Mechanical and Materials Engineering Department and Nebraska Center for Materials and Nanoscience, University of Nebraska−Lincoln, Lincoln, Nebraska 68588, United States;* ⓘ orcid.org/0000-0002-1792-7350

Steve R. Lustig − *U.S. Army Research Laboratory, Weapons and Materials Research Directorate, Aberdeen Proving Ground, Maryland 21005, United States; Department of Chemical Engineering, Northeastern University, Boston, Massachusetts 02115, United States;* ⓘ orcid.org/0000-0001-5030-852X

Complete contact information is available at:
https://pubs.acs.org/10.1021/acsami.9b23459

Author Contributions

#These authors contributed equally to this work.

Notes

The authors declare no competing financial interest.

interpreted as representing the official policies, either expressed implied, of the United States Merchant Marine Academy, the U.S. Department of Transportation, the Army Research Laboratory or the U.S. Government. The U.S. Government is authorized to reproduce and distribute reprints for Government purposes notwithstanding any copyright notation herein.

REFERENCES

(1) Hancox, N. L. *Mater. Eng.* **1993**, *14*, 312.

(2) Sawyer, L. C.; Chen, R. T.; Jamieson, M. G.; Musselman, I. H.; Russell, P. E. The Fibrillar Hierarchy in Liquid Crystalline Polymers. *J. Mater. Sci.* **1993**, *28* (1), 225−238.

(3) Smith, P.; Lemstra, P. J. Ultra-High-Strength Polyethylene Filaments by Solution Spinning/Drawing. *J. Mater. Sci.* **1980**, *15* (2), 505−514.

(4) Lemstra, P. J.; van Aerle, N. A. J. M.; Bastiaansen, C. W. M. Chain-Extended Polyethylene. *Polym. J.* **1987**, *19* (1), 85−98.

(5) Ran, S.; Fang, D.; Zong, X.; Hsiao, B. S.; Chu, B.; Cunniff, P. M. Structural Changes during Deformation of Kevlar® Fibers via On-Line Synchrotron SAXS/WAXD Techniques. *Polymer* **2001**, *42* (4), 1601−1612.

(6) Roenbeck, M. R.; Sandoz-Rosado, E. J.; Cline, J.; Wu, V.; Moy, P.; Afshari, M.; Reichert, D.; Lustig, S. R.; Strawhecker, K. E. Probing the Internal Structures of Kevlar® Fibers and Their Impacts on Mechanical Performance. *Polymer* **2017**, *128*, 200−210.

(7) Capaccio, G.; Ward, I. M. Preparation of Ultra-High Modulus Linear Polyethylenes; Effect of Molecular Weight and Molecular Weight Distribution on Drawing Behaviour and Mechanical Properties. *Polymer* **1974**, *15* (4), 233−238.

(8) Dobb, M. D.; Johnson, D. J.; Saville, B. P. Supramolecular Structure of a High-Modulus Polyaromatic Fiber (Kevlar® 49). *J. Polym. Sci., Polym. Phys. Ed.* **1977**, *15*, 2201−2211.

(9) Panar, M.; Avakian, P.; Blume, R. C.; Gardner, K. H.; Gierke, T. D.; Yang, H. H. Morphology of Poly(p-Phenylene Terephthalamide) Fibers. *J. Polym. Sci., Polym. Phys. Ed.* **1983**, *21*, 1955−1969.

(10) Fu, Y.; Chen, W.; Pyda, M.; Londono, D.; Annis, B.; Böller, A.; Habenschuss, A.; Cheng, J.; Wunderlich, B. Structure-Property Analysis for Gel-Spun, Ultrahigh Molecular Mass Polyethylene Fibers. *J. Macromol. Sci., Part B: Phys.* **1996**, *35* (1), 37−87.

(11) Berger, L.; Kausch, H. H.; Plummer, C. J. G. Structure and Deformation Mechanisms in UHMWPE-Fibres. *Polymer* **2003**, *44* (19), 5877−5884.

(12) Litvinov, V. M.; Xu, J.; Melian, C.; Demco, D. E.; Möller, M.; Simmelink, J. Morphology, Chain Dynamics, and Domain Sizes in Highly Drawn Gel-Spun Ultrahigh Molecular Weight Polyethylene Fibers at the Final Stages of Drawing by SAXS, WAXS, and 1H Solid-State NMR. *Macromolecules* **2011**, *44* (23), 9254−9266.

(13) Strawhecker, K. E.; Sandoz-Rosado, E. J.; Stockdale, T. A.; Laird, E. D. Interior Morphology of High-Performance Polyethylene Fibers Revealed by Modulus Mapping. *Polymer* **2016**, *103*, 224−232.

(14) Sawyer, L.; Jaffe, M. *High Performance Fibers*; Baer, E., Moet, A., Eds.; Hanser: New York, 1991.

(15) Morgan, R. J.; Pruneda, C. O. The Characterization of the Chemical Impurities in Kevlar® 49 Fibres. *Polymer* **1987**, *28* (2), 340−346.

(16) Wang, W.; Ruland, W.; Cohen, Y. Fibrillar and Microfibrillar Structures in Poly(P-phenylene Terephthalamide) Fibers. *Acta Polym.* **1993**, *44* (6), 273−278.

(17) McDaniel, P. B.; Strawhecker, K. E.; Deitzel, J. M.; Gillespie, J. W. Nanoscale Interfibrillar Adhesion in UHMWPE Fibers. *J. Polym. Sci., Part B: Polym. Phys.* **2018**, *56* (5), 391−401.

(18) Cheng, M.; Chen, W.; Weerasooriya, T. Experimental Investigation of the Transverse Mechanical Properties of a Single Kevlar® KM2 Fiber. *Int. J. Solids Struct.* **2004**, *41* (22−23), 6215−6232.

(19) Cheng, M.; Chen, W.; Weerasooriya, T. Mechanical Properties of Kevlar® KM2 Single Fiber. *J. Eng. Mater. Technol.* **2005**, *127* (2), 197−203.

(20) Hudspeth, M.; Nie, X.; Chen, W. Dynamic Failure of Dyneema SK76 Single Fibers under Biaxial Shear/Tension. *Polymer* **2012**, *53* (24), 5568−5574.

(21) Sockalingam, S.; Bremble, R.; Gillespie, J. W.; Keefe, M. Transverse Compression Behavior of Kevlar® KM2 Single Fiber. *Composites, Part A* **2016**, *81*, 271−281.

(22) McDaniel, P. B.; Sockalingam, S.; Deitzel, J. M.; Gillespie, J. W.; Keefe, M.; Bogetti, T. A.; Casem, D. T.; Weerasooriya, T. The Effect of Fiber Meso/Nanostructure on the Transverse Compression Response of Ballistic Fibers. *Composites, Part A* **2017**, *94*, 133−145.

(23) Staniszewski, J. M.; Sockalingam, S.; Bogetti, T. A.; Gillespie, J. W. Modeling the Fibrillation of Kevlar® KM2 Single Fibers Subjected to Transverse Compression. *Fibers Polym.* **2018**, *19* (7), 1479−1489.

(24) Grujicic, M.; Snipes, J. S.; Ramaswami, S. Multi-Scale Computational Analysis of the Nano-Indentation and Nano-Scratch Testing of Kevlar® 49 Single Fibers. *Proc. Inst. Mech. Eng., Part L* **2018**, *232* (6), 495−513.

(25) Oliver, W. C.; Pharr, G. M. An Improved Technique for Determining Hardness and Elastic Modulus Using Load and Displacement Sensing Indentation Experiments. *J. Mater. Res.* **1992**, *7*, 1564−1583.

(26) McAllister, Q. P.; Gillespie, J. W.; Vanlandingham, M. R. Nonlinear Indentation of Fibers. *J. Mater. Res.* **2012**, *27* (1), 197−213.

(27) McAllister, Q. P.; Gillespie, J. W.; Vanlandingham, M. R. The Influence of Surface Microstructure on the Scratch Characteristics of Kevlar® Fibers. *J. Mater. Sci.* **2013**, *48* (3), 1292−1302.

(28) Cole, D. P.; Strawhecker, K. E. An Improved Instrumented Indentation Technique for Single Microfibers. *J. Mater. Res.* **2014**, *29* (9), 1104−1112.

(29) Strawhecker, K. E.; Cole, D. P. Morphological and Local Mechanical Surface Characterization of Ballistic Fibers via AFM. *J. Appl. Polym. Sci.* **2014**, *131* (19), 1−12.

(30) Morgan, R. J.; Pruneda, C. O.; Steele, W. J. The Relationship between the Physical Structure and the Microscopic Deformation and Failure Processes of Poly(p-Phenylene Terephthalamide) Fibers. *J. Polym. Sci., Polym. Phys. Ed.* **1983**, *21* (9), 1757−1783.

(31) Dobb, M. G.; Robson, R. M. Structural Characteristics of Aramid Fibre Variants. *J. Mater. Sci.* **1990**, *25* (1), 459−464.

(32) Singletary, J.; Davis, H.; Song, Y.; Ramasubramanian, M. K.; Knoff, W. Transverse Compression of PPTA Fibers. Part II. Fiber Transverse Structure. *J. Mater. Sci.* **2000**, *35* (3), 583−592.

(33) Chabi, S.; Dikin, D. A.; Yin, J.; Percec, S.; Ren, F. Structure-Mechanical Property Relations of Skin-Core Regions of Poly(p-Phenylene Terephthalamide) Single Fiber. *Sci. Rep.* **2019**, *9* (1), 740.

(34) McAllister, Q. P.; Gillespie, J. W.; VanLandingham, M. R. Evaluation of the Three-Dimensional Properties of Kevlar® across Length Scales. *J. Mater. Res.* **2012**, *27* (14), 1824−1837.

(35) McDaniel, P. B.; Deitzel, J. M.; Gillespie, J. W. Structural Hierarchy and Surface Morphology of Highly Drawn Ultra High Molecular Weight Polyethylene Fibers Studied by Atomic Force Microscopy and Wide Angle X-Ray Diffraction. *Polymer* **2015**, *69*, 148−158.

(36) Gindl, W.; Gupta, H. S. Cell-Wall Hardness and Young's Modulus of Melamine-Modified Spruce Wood by Nano-Indentation. *Composites, Part A* **2002**, *33* (8), 1141−1145.

(37) Konnerth, J.; Gindl, W. Mechanical Characterisation of Wood-Adhesive Interphase Cell Walls by Nanoindentation. *Holzforschung* **2006**, *60* (4), 429−433.

(38) Jakes, J. E.; Frihart, C. R.; Beecher, J. F.; Moon, R. J.; Stone, D. S. Experimental Method to Account for Structural Compliance in Nanoindentation Measurements. *J. Mater. Res.* **2008**, *23* (4), 1113−1127.

(39) Stockdale, T. A.; Strawhecker, K. E.; Sandoz-Rosado, E. J.; Wetzel, E. D. A Rapid FIB-Notch Technique for Characterizing the Internal Morphology of High-Performance Fibers. *Mater. Lett.* **2016**, *176*, 173−176.

(40) Sandoz-Rosado, E.; Roenbeck, M. R.; Strawhecker, K. E. Quantifying High-Performance Material Microstructure Using Nanomechanical Tools with Visual and Frequency Analysis. *Scanning* **2018**, *2018*, 1−12.

(41) Roenbeck, M. R.; Cline, J.; Wu, V.; Afshari, M.; Kellner, S.; Martin, P.; Londono, J. D.; Clinger, L. E.; Reichert, D.; Lustig, S. R.; Strawhecker, K. E. Structure-Property Relationships of Aramid Fibers via X-Ray Scattering and Atomic Force Microscopy. *J. Mater. Sci.* **2019**, *54*, 6668−6683.

(42) Volkert, C. A.; Minor, A. M. Focused Ion Beam Micromachining. *MRS Bull.* **2007**, *32*, 389−399.

(43) McDaniel, P. B.; Deitzel, J. M.; Gregory, D.; Polakovic, T.; Gillespie, J. W. Single Fiber Peel Test to Assess Ultra High Molecular Weight Polyethylene Fiber Mesostructure Interactions. *J. Appl. Polym. Sci.* **2018**, *135* (16), 46156.

(44) Stone, D. S.; Yoder, K. B.; Sproul, W. D. Hardness and Elastic Modulus of TiN Based on Continuous Indentation Technique and New Correlation. *J. Vac. Sci. Technol., A* **1991**, *9* (4), 2543.

(45) Schindelin, J.; Arganda-Carreras, I.; Frise, E.; Kaynig, V.; Longair, M.; Pietzsch, T.; Preibisch, S.; Rueden, C.; Saalfeld, S.; Schmid, B.; Tinevez, J.; White, D.; Hartenstein, V.; Eliceiri, K.; Tomancak, P.; Cardona, A. Fiji: An Open-Source Platform for Biological-Image Analysis. *Nat. Methods* **2012**, *9*, 676.

(46) Rueden, C. T.; Schindelin, J.; Hiner, M. C.; DeZonia, B. E.; Walter, A. E.; Arena, E. T.; Eliceiri, K. W. ImageJ2: ImageJ for the next Generation of Scientific Image Data. *BMC Bioinf.* **2017**, *18* (1), 529.

(47) Oliver, W. C.; Pharr, G. M. Measurement of Hardness and Elastic Modulus by Instrumented Indentation: Advances in Understanding and Refinements to Methodology. *J. Mater. Res.* **2004**, *19* (1), 3−20.

(48) Sneddon, I. N. The Relation between Load and Penetration in the Axisymmetric Boussinesq Problem for a Punch of Arbitrary Profile. *Int. J. Eng. Sci.* **1965**, *3* (1), 47−57.

(49) McAllister, Q. P.; Gillespie, J. W.; Vanlandingham, M. R. The Sub-Micron Scale Energy Dissipative Deformation Mechanisms of Kevlar® Fibrils. *J. Mater. Sci.* **2013**, *48* (18), 6245−6261.

(50) Ohta, Y.; Murase, H.; Hashimoto, T. Structural Development of Ultra-High Strength Polyethylene Fibers: Transformation from Kebabs to Shishs through Hot-Drawing Process of Gel-Spun Fibers. *J. Polym. Sci., Part B: Polym. Phys.* **2010**, *48* (17), 1861−1872.

(51) Wang, Z.; An, M.; Xu, H.; Lv, Y.; Tian, F.; Gu, Q. Structural Evolution from Shish-Kebab to Fibrillar Crystals during Hot-Stretching Process of Gel Spinning Ultra-High Molecular Weight Polyethylene Fibers Obtained from Low Concentration Solution. *Polymer* **2017**, *120*, 244−254.

(52) Blades, H. Dry-Jet Wet Spinning Process, *Polymer*, **1973**, *42*, 10087.

(53) Picken, S. J.; Sikkema, D. J.; Boerstoel, H.; Dingemans, T. J.; van der Zwaag, S. Liquid Crystal Main-Chain Polymers for High-Performance Fibre Applications. *Liq. Cryst.* **2011**, *38* (11−12), 1591−1605.

(54) Hoogsteen, W.; Ten Brinke, G.; Pennings, A. J. SAXS Experiments on Voids in Gel-Spun Polyethylene Fibres. *J. Mater. Sci.* **1990**, *25* (3), 1551−1556.

(55) Hu, W. G.; Schmidt-Rohr, K. Characterization of Ultradrawn Polyethylene Fibers by NMR: Crystallinity, Domain Sizes and a Highly Mobile Second Amorphous Phase. *Polymer* **2000**, *41* (8), 2979−2987.

(56) Jackson, C. L.; Schadt, R. J.; Gardner, K. H.; Chase, D. B.; Allen, S. R.; Gabara, V.; English, A. D. Dynamic Structure and Aqueous Accessibility of Poly(p-Phenylene Terephthalamide) Crystallites. *Polymer* **1994**, *35* (6), 1123−1131.

(57) Chatzi, E. G.; Ishida, H.; Koenig, J. L. FT-IR Study of the Water Absorbed in Kevlar®-49 Fibers. *Appl. Spectrosc.* **1986**, *40* (6), 847−851.

(58) Mathur, A.; Netravali, A. N. Modification of Mechanical Properties of Kevlar® Fibre by Polymer Infiltration. *J. Mater. Sci.* **1996**, *31*, 1265−1274.

(59) Wang, W.; Ruland, W.; Cohen, Y. Fibrillar and Microfibrillar Structures in Poly(p-Phenylene Terephthalamide) Fibers. *Acta Polym.* **1993**, *44* (6), 273−278.

(60) Hindeleh, A. M.; Abdo, S. M. Effects of Annealing on the Crystallinity and Microparacrystallite Size of Kevlar® 49 Fibres. *Polymer* **1989**, *30* (2), 218−224.

(61) Uppal, R.; Ramaswamy, G. N.; Loughin, T. A Novel Method to Assess Degree of Crystallinity of Aramid Filament Yarns. *J. Ind. Text.* **2013**, *43* (1), 3−19.

(62) Kanamoto, T.; Tanaka, K.; Takeda, M.; Tsuruta, A.; Porter, R. S. Superdrawing of Ultrahigh Molecular Weight Polyethylene. 1. Effect of Techniques on Drawing of Single Crystal Mats. *Macromolecules* **1988**, *21* (2), 470−477.

(63) Garcia-Leiner, M.; Song, J.; Lesser, A. J. Drawing of Ultrahigh Molecular Weight Polyethylene Fibers in the Presence of Supercritical Carbon Dioxide. *J. Polym. Sci., Part B: Polym. Phys.* **2003**, *41* (12), 1375−1383.

(64) McGarry, F. J.; Moalli, J. E. Mechanical Behaviour of Rigid Rod Polymer Fibres: 1. Measurement of Axial Compressive and Transverse Tensile Properties. *Polymer* **1991**, *32* (10), 1811−1815.

(65) Launey, M. E.; Buehler, M. J.; Ritchie, R. O. *Annu. Rev. Mater. Res.;* **2010**, *40*, 25.

(66) Galanov, B. A. Similarity Approach to Hertz Type Contact Problems. In *IUTAM Symposium on Scaling in Solid Mechanics*; Borodich, F. M., Ed.; 2009; Vol. *10*, pp 111−122 DOI: 10.1007/978-1-4020-9033-2.

(67) Dzenis, Y. A.; Reneker, D. H.; Tsukruk, V. V.; Patil, R. Fractal Analysis of Surfaces of Advanced Reinforcing Fibers by Atomic Force Microscopy. *Compos. Interfaces* **1994**, *2* (4), 307−319.

(68) Dzenis, Y. A.; Joshi, S. P. Inhomogeneous Anisotropic Percolation: Two-Dimensional Numerical Threshold Analysis. *Phys. Rev. B: Condens. Matter Mater. Phys.* **1994**, *49* (5), 3566−3568.

(69) Borodich, F. M. Fractals and Fractal Scaling in Fracture Mechanics. *Int. J. Fract.* **1999**, *95* (1−4), 239−259.

Supporting Information for

Hierarchical Mechanisms of Lateral Interactions in High-Performance

Fibers

Taylor A. Stockdale[1], Daniel P. Cole[2], Jeffrey M. Staniszewski[3], Michael R. Roenbeck[3],

Dimitry Papkov[1,4], Steve R. Lustig[5], Yuris A. Dzenis[1]*, Kenneth E. Strawhecker[3]*

[1] Mechanical and Materials Engineering Department, University of Nebraska-Lincoln, Lincoln, NE 68588,

USA

[2] U.S. Army Research Laboratory, Vehicle Technology Directorate, Aberdeen Proving Ground, MD 21005,

USA

[3] U.S. Army Research Laboratory, Weapons and Materials Research Directorate, Aberdeen Proving

Ground, MD 21005, USA

[4] Nebraska Center for Materials and Nanoscience, University of Nebraska-Lincoln, Lincoln, NE 68588, USA

[5] Department of Chemical Engineering, Northeastern University, Boston, MA 02115, USA

*E-mail correspondence to: kenneth.e.strawhecker.civ@mail.mil, ydzenis@unl.edu

Statistical Analysis

Statistical analysis was performed, using SAS® Proc Glimmix software, Version 9.2 TS of the SAS System for Windows. Copyright ©2002-2008 SAS Institute Inc. SAS and all other SAS Institute Inc. product or service names are registered trademarks or trademarks of SAS Institute Inc., Cary, NC, USA. $\alpha = 0.1$ statistical significance level was used. In all statistical models, variation between different fibers of the same materials was treated as a random effect.

Regression analysis

In regression analysis indentation depth was considered a quantitative independent variable, and a fixed effects model of the following type was used:

$$Property = (material + ind\_depth) + (material * ind\_depth)$$

where property refers to hardness, max load, etc., and the material*ind_depth is the interaction term. In cases where the interaction term was statistically significant, main effects were retained.

Figures S1 – S3 show the scatterplots for the different properties. Each of the

figures is broken into panels by fiber material. For each of the models, the first step

examined the statistical significance of each of the parameters in the model. Where

needed, the model was reduced before the final fit. Table S1 summarizes the test for

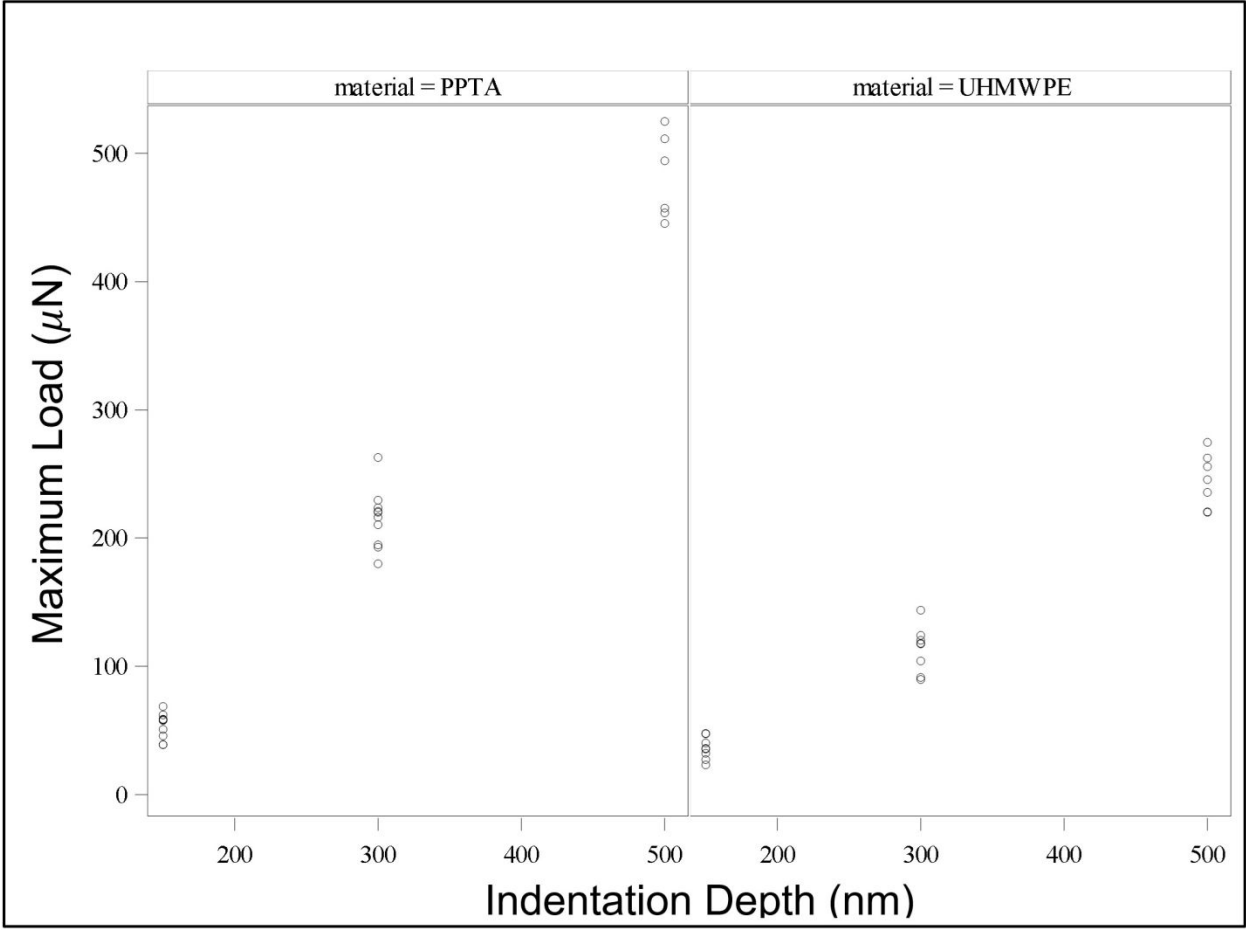statistical significance in the different linear models.

Figure S1: Scatter plots for sample maximum load at each indentation depth for PPTA (left) and UHMWPE (right).
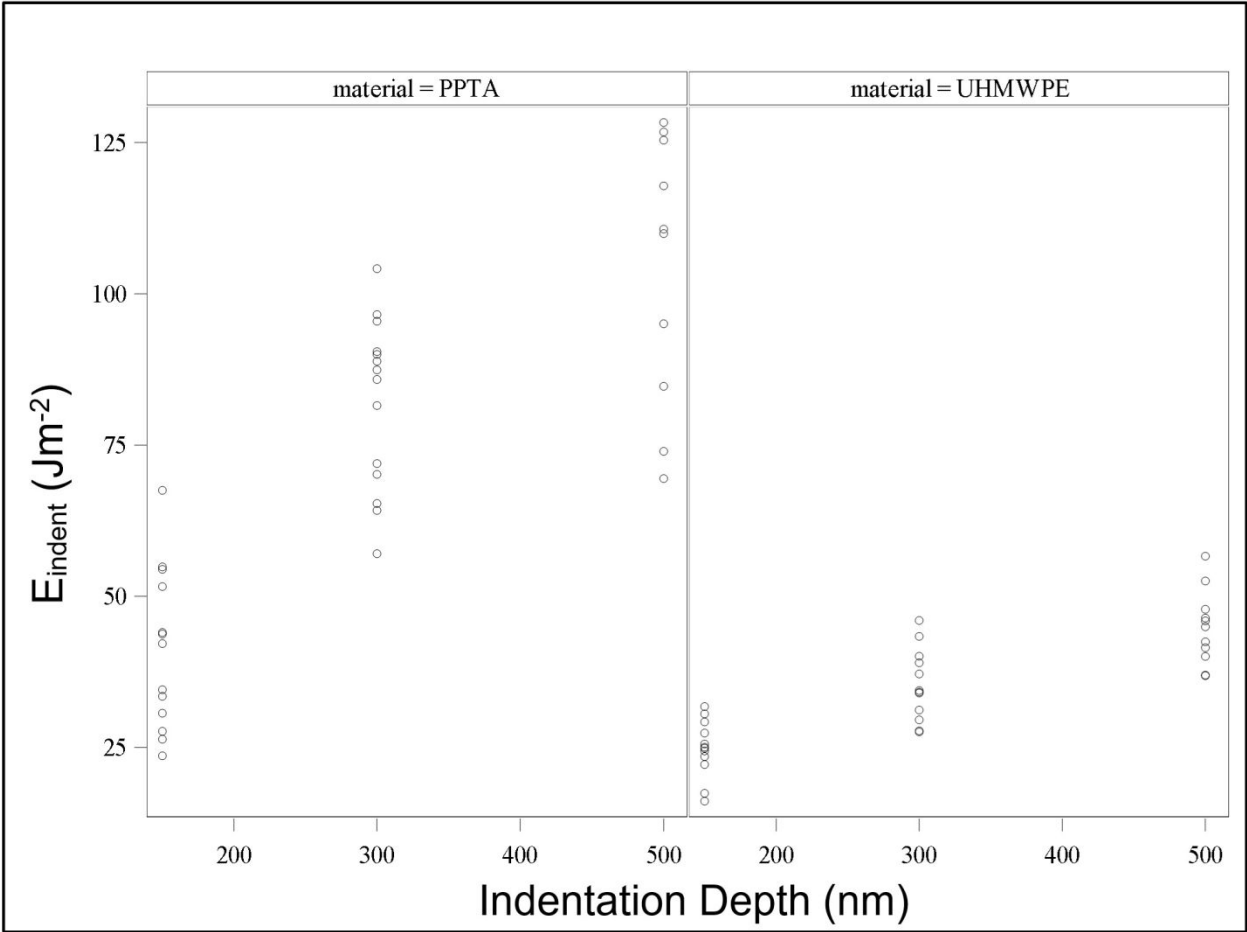
Figure S2: Scatter plots for sample indentation energy from single indents performed at each indentation depth for PPTA (left) and UHMWPE (right).
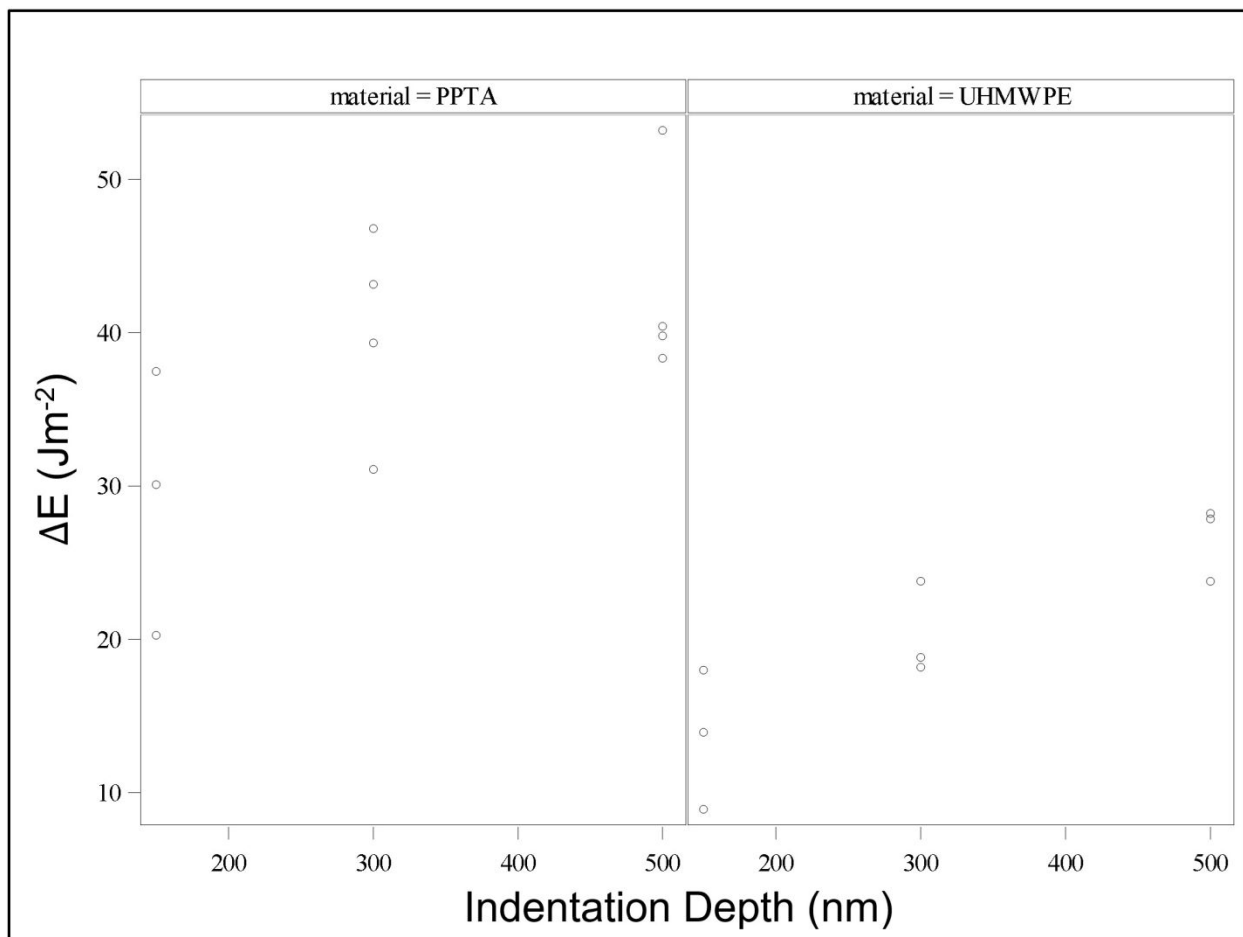
Figure S3: Scatter plots for sample absorbed energy from repeated indents at each indentation depth for PPTA (left) and UHMWPE (right).

Table S1: Type 1 test for statistical significance of the fixed effects of the different parameters in the linear models. The shaded areas in the table mark the P-values of the different parameters

| | Type I Tests of Fixed Effects | | | | | | | | | | | |
| Effect | Maximum Load | | | | E_{indent} | | | | ΔE | | | |
	Num DF	Den DF	F Value	Pr > F	Num DF	Den DF	F Value	Pr > F	Num DF	Den DF	F Value	Pr > F
material	1	2	61.3	0.016	1	2	157.6	0.006	1	2	45.61	0.021
ind_depth	1	43	1871.0	$<10^{-4}$	1	66	111.5	$<10^{-4}$	1	14	15.15	0.002
ind_depth*material	1	43	214.1	$<10^{-4}$	1	66	30.7	$<10^{-4}$	1	14	0.00	0.968

In the models for maximum load and E_{indent}, all parameters in the model were retained since all the main effects and interactions were statistically significant at the α = 0.1 confidence level. In the case of ΔE, the interaction parameter was not statistically significant and the model was reduced to:

$$\Delta E = material + ind\_depth$$

Table S2 – S4 summarize the fitted parameters for the linear models, and Table S5 summarizes the obtained formulas for the regression lines:

Table S2: Fitted parameters and the corresponding 90% CIs for the linear model for maximum load fit (the shaded rectangle marks the CIs for the slopes). None of the CIs contains zero and thus the slopes are statistically significant.

Solutions for Fixed Effects									
Effect	material	Estimate	Standard Error	DF	t Value	Pr > |t|	Alpha	Lower	Upper
Material	PPTA	-136.1	11.7	2	-11.65	0.007	0.1	-170.2	-102.0
Material	UHMWPE	-59.8	12.3	2	-4.88	0.04	0.1	-95.6	-24.0
ind_dep(material)	PPTA	1.22	0.030	43	40.97	<.0001	0.1	1.165	1.265
ind_dep(material)	UHMWPE	0.60	0.030	43	20.17	<.0001	0.1	0.550	0.651

Table S3: Fitted parameters and the corresponding 90% CIs for the linear model for E_{indent} fit (the shaded rectangle marks the CIs for the slopes). Again, none of the CIs contains zero and thus the slopes are statistically significant.

Solutions for Fixed Effects									
Effect	material	Estimate	Standard Error	DF	t Value	Pr > |t|	Alpha	Lower	Upper
Material	PPTA	19.5	5.24	2	3.72	0.065	0.1	4.18	34.76
Material	UHMWPE	17.1	5.36	2	3.19	0.086	0.1	1.46	32.79
ind_dep(material)	PPTA	0.18	0.016	66	11.37	<.0001	0.1	0.154	0.206
ind_dep(material)	UHMWPE	0.056	0.0157	66	3.60	0.0006	0.1	0.0303	0.0826

Table S4: Fitted parameters for the reduced model for ΔE (the shaded rectangle marks the P-value for the slope).

Solutions for Fixed Effects						
Effect	material	Estimate	Standard Error	DF	t Value	Pr > |t|
Material	PPTA	26.1	3.48	2	7.50	0.017
Material	UHMWPE	8.63	3.458	2	2.50	0.13
Ind_depth		0.036	0.0091	15	4.01	0.001

Table S5: Summary of the different fits for the linear models.

	Fit		
Sample	Maximum Load	E_{indent}	ΔE
PPTA	P_max = -136.1 + 1.22*ind_depth	E_{indent} = 19.5 + 0.18*ind_depth	ΔE = 26.1 + 0.036*ind_depth
UHMWPE	P_max = -59.8 + 0.60*ind_depth	E_{indent} = 17.1 + 0.056*ind_depth	ΔE = 8.63 + 0.036*ind_depth

Assumptions of equal variance and normality of residuals were tested for all fits. It

was not possible to test the assumptions for the ΔE model due to small number of tests.

Generally, the fits indicated no significant violations of the constant variance assumption

(top left panel in Figure S4 – S5). Minor deviations from the constant variance assumption

(with a mild funnel shape) were observed for maximum force and normalized indentation

energy fits. Small deviations from normality were observed in the QQ-plots (bottom left

panel in Figure S4 – S5) in some cases, they were minor and restricted to the lower and

upper ranges of the plot, with maximum force and normalized indentation energy
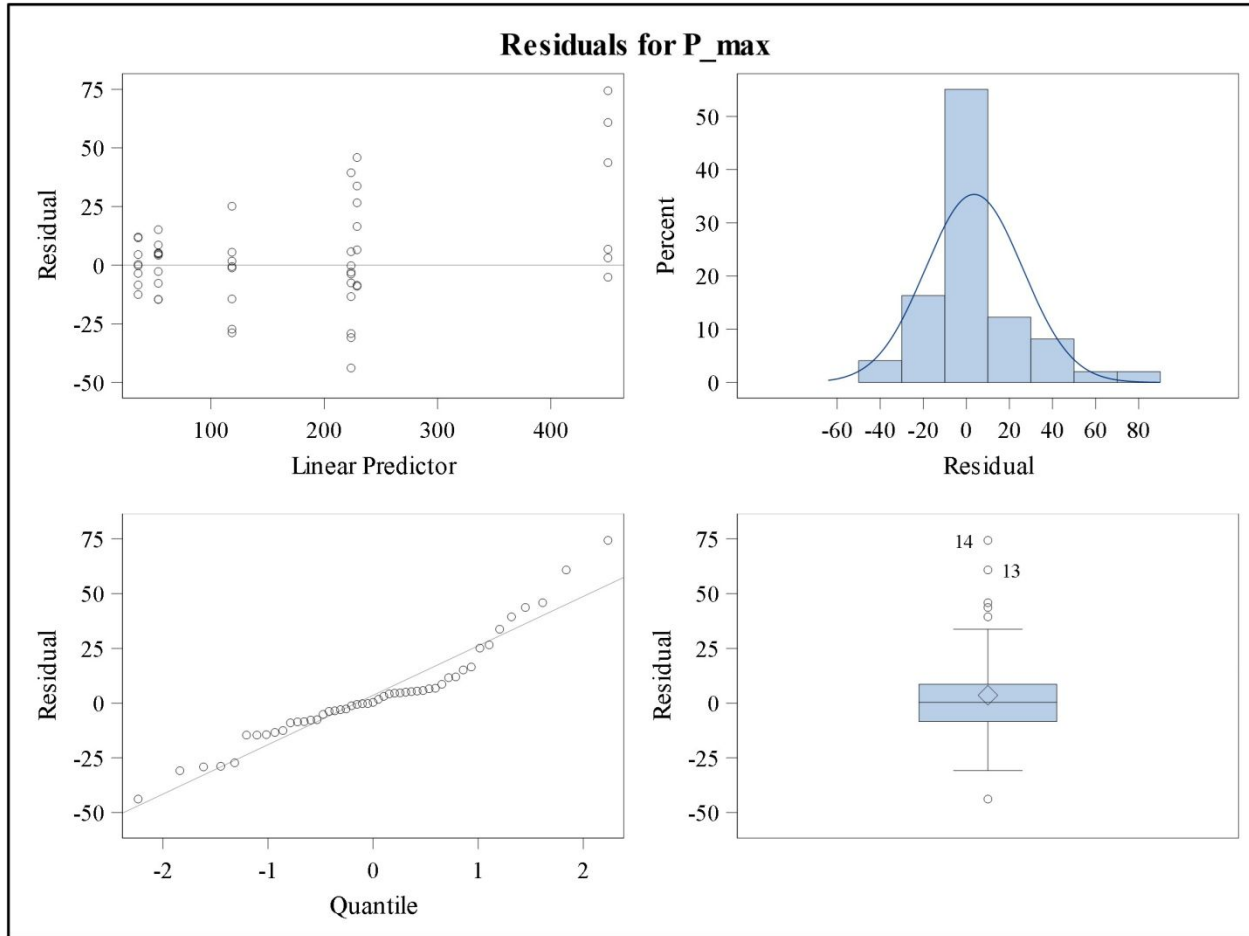
producing the largest deviations.

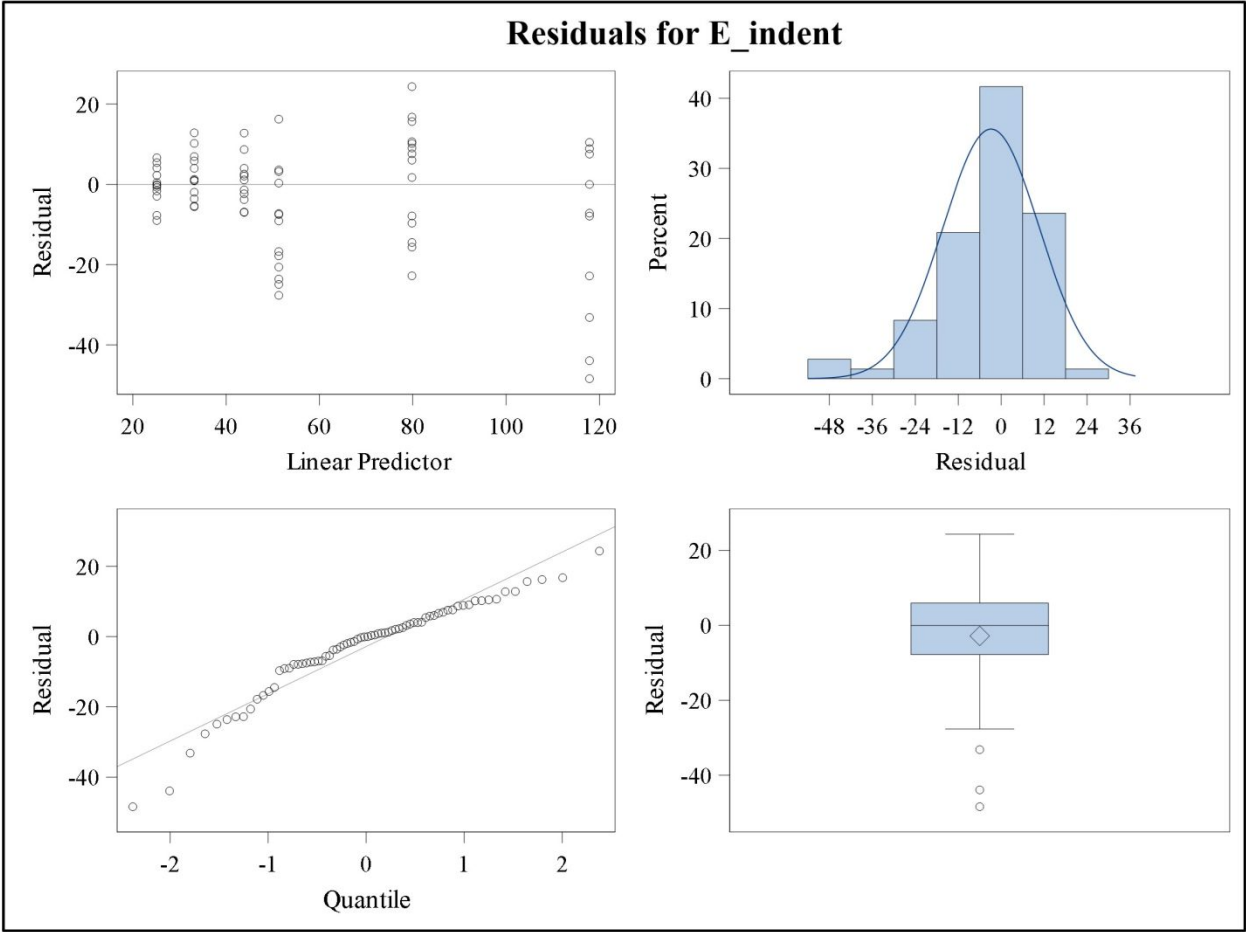Figure S4: Constant variance and normality test for the maximum load linear fit

Figure S5: Constant variance and normality test for E_indent linear fit

Structural Compliance Determination

Exposed internal surfaces were raster scanned using the indenter probe (Hysitron TI-950 Triboindenter) and features were identified in the obtained topography maps (10 – 15 μm scan size, 0.4 – 0.5 Hz scan rate, 1.0 μN setpoint). In the obtained images, see Figure S8a, several oriented fibril bundles are clearly distinguishable. Image sizes and scan locations were adjusted to maximize the capture area while avoiding the edge of the fiber. The FIB-notch left a visible etch on the surface of the glass vial, allowing the exposed internal surface of the fiber to be easily located. Following the procedure for measuring structural compliance by Jakes et al. [S1], three arrays of equally spaced indentations were performed across the width of each initially imaged location at set depths of 150, 300, and 500 nm, respectively. Quasi-static nanoindentation was conducted using a 60° sphero-conical diamond probe (350 nm tip radius) in displacement control. A triangular loading scheme was used with a 10 second loading segment followed by a 10 second unloading segment. An image of the fiber interior after performing the structural compliance indentations is shown in Figure S8b.

Image Scan Size: 11.000 µm
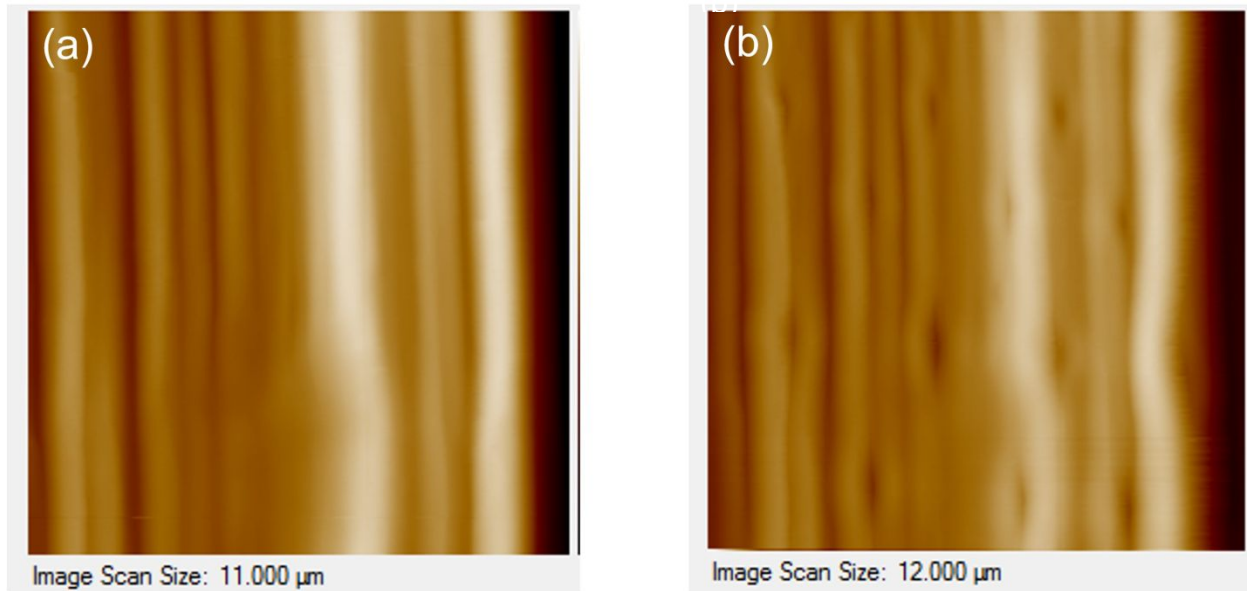
Image Scan Size: 12.000 µm

Figure S6: Representative image of the interior surface of a peeled UHMWPE fiber showing several oriented fibril bundles (a) and the same area after performing indents to determine structural compliance (b).

These indents were performed such that each radial location across the width of the imaged area had 3 indents at different depths. Using these three data points, a Stone, Yoder, Sproul (SYS) plot was generated by plotting the product of the total compliance and the root of the maximum load as a function of the root of the max load as shown in Equation S1

$$C_t\sqrt{P_{max}} = (C_m + C_s)\sqrt{P_{max}} + \sqrt{J} \tag{S1}$$

where C_t is the total compliance, P_{max} is the maximum load, C_m is the machine

compliance, which is a known quantity related to the instrument used for characterization,

C_s is the structural compliance and J is the Joslin-Oliver parameter defined as the

measured hardness divided by the square of the reduced modulus $\left(\frac{H}{E_r^2}\right)$. Thus, the

structural compliance can be extracted from the slope of a linear regression analysis

performed at each radial location. An example of an SYS plot is presented in Figure S9a.

After extracting the structural compliance from each linear regression curve, the structural

compliance is plotted as a function of radial position in the obtained image, as shown in

Figure S9b. From this plot, we indicate a region exhibiting the lowest structural

compliance, and subsequent indentations between fibril bundles are restricted to bundles
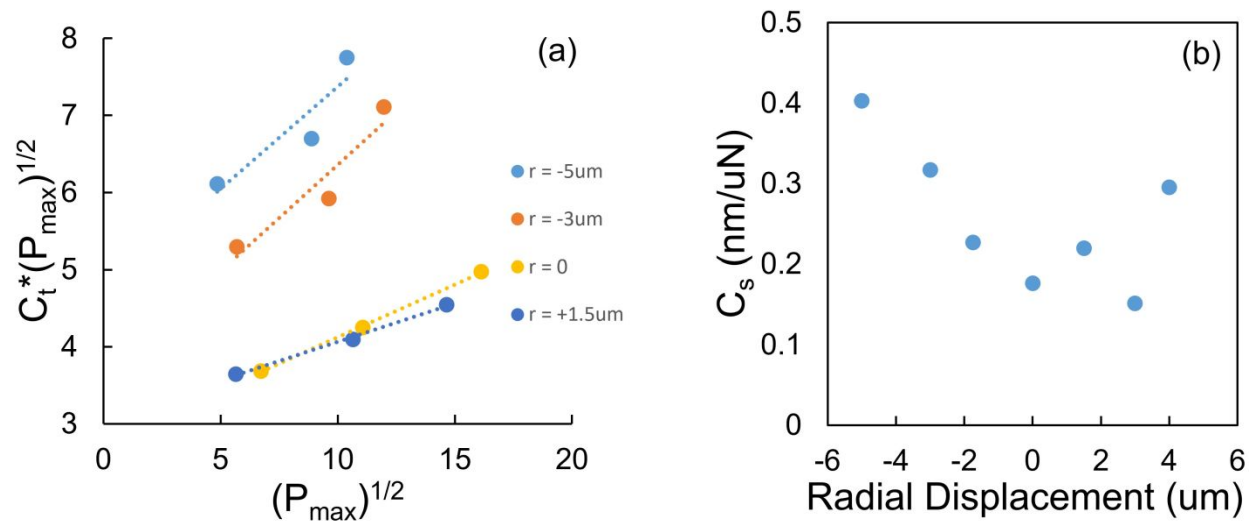
within this minimized compliance region.

Figure S7: Representative SYS plot with linear regression curves for different radial indent locations (a) and corresponding plot of structural compliance as a function of radial position (b). For this sample, the acceptable indentation region is between -2 – 3 μm from the center of the imaged area.

Finite Element Model Development

A 100 μm long section of a 12 μm diameter half cylinder on a rigid, fixed planar surface was modeled using half symmetry. The experimental boundary conditions were replicated by fixing the ends of the half-fiber section and defining frictionless contact between the fixed planar surface and the bottom the fiber. Frictionless contact was also defined between the probe tip, which was modeled rigidly with an area profile matching the experiment, and the exposed top surface of the half-fiber. The nanoindentation simulation was run using quasi-static, displacement-controlled boundary conditions in Abaqus®/Standard finite element analysis software. The mesh consisted of approximately 100,000 fully integrated, 3D hexahedral elements, with denser refinement for areas in immediate contact with the probe tip and planar surface. A sensitivity analysis on the modeled fiber length was conducted to ensure the results were free of effects from the fixed end boundary condition.

The transverse behavior of the modeled fiber is assumed to be elastic-plastic [S2,S3]. To account for the fiber mechanical properties, the model was calibrated using experimental results from 150 nm indents on a relatively flat area of a PPTA fiber with

minimized structural compliance. It should be noted that simulation results only consider the geometric implications of the indentation location. While the model simulates PPTA fibers, the only structural characteristics included are cylinder size (fiber diameter) and nanofibril bundle size (from surface profile scans), so results are expected to simply scale with the size of the model.

A similar structural compliance analysis was performed on a flat half cylinder, where indent simulations of 150, 300, and 500 nm depths were conducted at 0, 2.5, and 5 μm offset from the centerline of the fiber. Simulations showed a decrease in the reduced modulus due to offset from the centerline, with reductions between 14% for a 150 nm depth and 2.5 μm offset and 55% for a 500 nm depth and 5 μm offset. Using the measured structural compliance values at various radial positions, FEM models can be updated to better predict the indentation response based on indent location.

References

S1. Jakes, J. E.; Frihart, C. R.; Beecher, J. F.; Moon, R. J.; Stone, D. S. Experimental

Method to Account for Structural Compliance in Nanoindentation Measurements. *J.*

Mater. Res. **2008**, *23* (4), 1113-1127.

S2. Singletary, J.; Davis, H.; Song, Y.; Ramasubramanian, M. K.; Knoff, W. Transverse

Compression of PPTA Fibers. Part II. Fiber Transverse Structure. *J. Mater. Sci.*

2000, *35*, 583-592.

S3. Sockalingam, S.; Bremble, R.; Gillespie, J.W.; Keefe, M. Transverse Compression

Behavior of Kevlar KM2 Single Fiber. *Compos. Part A Appl. Sci. Manuf.* **2016**, *81*,

271-281.